# Effective k · p model of monolayer 1$T'$-$MoS_2$ under perpendicular electric field

Ma Zhou,[1] Sheng-bin Yu,[2] An-hua Huang,[2] Li Wang,[1] and Kai Chang[2,*]
[1]*School of Physics and Materials Science, Nanchang University, Nanchang 330031, China*
[2]*SKLSM, Institute of Semiconductors, Chinese Academy of Sciences, P.O. Box 912, Beijing 100083, China*

(Received 16 December 2022; accepted 28 June 2023; published 18 July 2023)

We derive the effective **k** · **p** Hamiltonian for an electron in monolayer $T'$-$MoS_2$ near the Fermi level in the presence of spin-orbit coupling and a perpendicular electric field. The $4 \times 4$ **k** · **p** Hamiltonian is capable of describing the nonparabolic energy band dispersion, perpendicular electric field effect, and spin texture, in good agreement with first-principles calculations. This **k** · **p** Hamiltonian provides a simple and convenient way to understand and manipulate the spin transport properties of monolayer $T'$-$MoS_2$ under the perpendicular electric field. Surprisingly, our model predicts a significantly large out-of-plane spin polarization ($S_z$) induced by the charge current along the $x$ direction. We also prove that the mirror symmetry ($\sigma_h(yz)$) leads to the forbidden of spin polarization ($S_z$) induced by the charge current along the $y$ direction.

DOI: 10.1103/PhysRevB.108.035412

## I. INTRODUCTION

The discovery of graphene has triggered a great leap in the research on monolayer two-dimensional (2D) materials [1]. A decade of intense research on fabricating 2D atomic crystals has revealed many three-dimensional (3D) van der Waals solids [2–5]. All these 2D materials can be broadly classified into two types: (1) 2D material with weak spin orbit coupling (SOC), e.g., graphene [1] and phosphorene [3], and (2) 2D material with strong SOC, e.g., monolayer indium selenides [4]. The 2D materials with strong SOC provide a great platform for spin transport research.

In 2010 experiments demonstrated that $MoS_2$, a prototypical group-VI dichalcogenide, crosses over from an indirect-gap semiconductor at multilayers to a direct band-gap one at a monolayer [6]. In 2012 Yao showed that inversion symmetry breaking together with strong SOC lead to coupled spin and valley physics in monolayer $MoS_2$ and other group VI dichalcogenides, making possible spin and valley control in these 2D materials [7]. The spin transport properties of monolayer $MoS_2$ have since been investigated by many researchers in theory and experiments. In 2013 Ochoa and Roldán theoretically studied the intravalley spin-orbit-mediated spin relaxation in monolayer $MoS_2$. By using a two-band spin-dependent Hamiltonian, they obtained the spin lifetimes in monolayer $MoS_2$ larger than nanoseconds [8], which is in agreement with the valley polarization experiment [9]. Since the monolayer $MoS_2$ has mirror symmetry $\sigma_h$, there is no Rashba spin-orbit coupling (RSOC) unless the $\sigma_h$ symmetry is expressly broken by the perpendicular electric field (PEF). In 2018 Taguchi theoretically predicted the emergence of the Edelstein effect, namely, current-induced spin polarization (CISP), in gated monolayer $MoS_2$, where the mirror symmetry $\sigma_h$ is broken by the PEF [10]. All the theoretical studies related to the spin transport phenomenon listed above are based on a reliable spin-dependent effective Hamiltonian, which can be used to describe the spin texture near the Fermi surface. Therefore, the development of spin-dependent effective Hamiltonian is of great significance for the 2D material with strong SOC, such as monolayer $MoS_2$.

In 2014 using a first-principles calculation, Qian and Li predicted a class of large-gap quantum spin Hall insulators in 2D transition metal dichalcogenides with 1$T'$ structure, 1$T'$-$MX_2$ with M = (W, Mo) and X = (Te, Se, S) [11]. They developed a $4 \times 4$ **k** · **p** Hamiltonian to describe the topological band structure, which leads to the quantum spin Hall effect. By using first-principles calculation, they also predicted that the PEF gives rise to the topological phase transition.

Besides monolayer 1$T'$-$MoS_2$, other researchers have investigated the transport properties of distorted monolayer $WTe_2$ [12,13]. For example, Lau *et al.* have constructed an accurate tight-binding model to describe the band structure of monolayer 1$T'$-$WTe_2$ [12]. Based on this model, they studied the topological edge state in monolayer 1$T'$-$WTe_2$. Apart from the monolayer 1$T'$-$WTe_2$, recent research has revealed that the 1$T_d$ phase of monolayer $WTe_2$ also exhibits some remarkable properties. In 2020 Garcia *et al.* developed an effective **k** · **p** Hamiltonian to describe the electronic structure of monolayer 1$T_d$-$WTe_2$ [13]. By using this **k** · **p** Hamiltonian, they studied the spin Hall effect in 1$T_d$-$WTe_2$. Hu and Liu constructed a realistic four-band tight-binding (TB) model for monolayer 1$T'$-$MX_2$ (M = Mo, W and X = Te, Se, S) by combining the symmetry analysis and first-principles calculations [14].

Although there are already quite a few simplified model Hamiltonians available for describing the electronic structure of monolayer distorted $MX_2$ [11–13], no effective **k** · **p** Hamiltonian has been developed to describe the PEF effect on spin texture and band dispersion of monolayer 1$T'$-$MoS_2$.

*Corresponding author: kchang@semi.ac.cn

 ©2023 American Physical Society

Here we derive the effective $\mathbf{k}\cdot\mathbf{p}$ Hamiltonian to describe the monolayer $T'$-$MoS_2$ electronic structure in the presence of SOC and the PEF. With two conduction bands and two valence bands in the vicinity of the band gap included, our $\mathbf{k}\cdot\mathbf{p}$ Hamiltonian can describe not only the nonparabolic dispersion, but also the PEF-induced topological phase transition, in good agreement with the first-principles calculations. Significantly, our $\mathbf{k}\cdot\mathbf{p}$ Hamiltonian can also describe the effect of PEF on the spin texture, which decides the spin transport properties in $1T'$-$MoS_2$. Based on our $\mathbf{k}\cdot\mathbf{p}$ Hamiltonian, we calculate the CISP response and find that the PEF can give rise to a significantly large out-of-plane ($S_z$) spin polarization when there is a charge current along the $x$ direction. However, the $y$ direction charge current cannot induce out-of-plane ($S_z$) spin polarization. By using symmetry analysis, we conclude that the $y$ direction current ($J_y$) to out-of-plane ($S_z$) spin conversion is strictly forbidden since the $1T'$-$MoS_2$ has mirror symmetry $\sigma_h(yz)$.

The rest of this paper is organized as follows. In Sec. II the effective $\mathbf{k}\cdot\mathbf{p}$ Hamiltonian which can be used to describe the PEF effect on band dispersion and spin texture is directly given. In Sec. III we calculate the CISP of the monolayer $1T'$-$MoS_2$ based on our $\mathbf{k}\cdot\mathbf{p}$ Hamiltonian. Here our calculations have already taken into account the disorder effect and obtain the charge-to-spin conductivity with different PEF for different disorder strengths. The summary and final conclusions are in Sec. IV.

## II. EFFECTIVE HAMILTONIAN OF MONOLAYER $T'$ TRANSITION METAL DICHALCOGENIDES

The electronic structures of the monolayer $1T'$-$MoS_2$ are calculated utilizing the Vienna Ab Initio Simulation Package (VASP) code [15,16] based on density-functional theory (DFT) [17,18]. The electron exchange-correlation functional is treated within the generalized gradient approximation (GGA) of Perdew-Burke-Ernzerhof (PBE) [19] and projected augmented wave (PAW) [20]. We set the kinetic energy cutoff to 500 eV for the wave function expansion, and the $k$-point grid is sampled by sums over $16\times16\times1$. The electronic self-consistent calculations converge up to a precision of $10^{-8}$ eV in total energy difference. The Gaussian smearing method with a width of 0.05 eV was employed. A slab model, together with a vacuum layer larger than 20 Å, was employed. The equilibrium crystal structure is taken by fully atomic relaxation with the maximum force on each atom less than 0.01 eV/Å. The calculated lattice parameters of the $T'$-$MoS_2$ are $R_x = 3.17$ Å, $R_y = 5.72$ Å [Fig. 1(a)]. As we can see in Fig. 1, the Mo atoms are located in the $xy$ plane. The $S_1(S_2)$ atom is located 0.0566 Å (0.0740 Å) away from the $xy$ plane in the perpendicular direction. The vectors labeled in Fig. 1(a) ($\mathbf{d_0}-\mathbf{d_2}$) are $\mathbf{d_0} = [0, 2.1810, 0.0535]$ Å, $\mathbf{d_1} = [1.5871, 2.2629, 0.0063]$ Å, $\mathbf{d_2} = [1.5871, -1.2813, 0.0598]$ Å, and $\mathbf{d_3} = [1.5871, -0.8997, -0.1133]$ Å.

Our numerical results shown in Figs. 2(a) and 2(b) are in good agreement with the DFT-PBE results obtained in previous work [11,14]. As we can see in Fig. 2(a), the lowest conduction and highest valence band are nonparabolic and the band gap is located around $\pm\Lambda \approx \pm(0.17, 0)$ Å$^{-1}$ [red dots in Fig. 1(c)]. Here we define the $K$ ($K'$) valley located

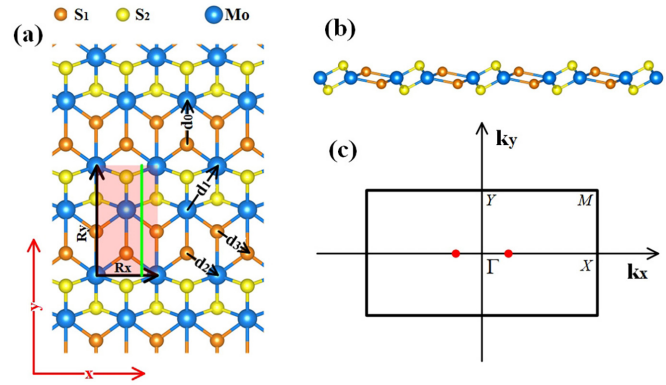


FIG. 1. Crystal structure of monolayer $T'$-$MoS_2$. (a) Top view and (b) side view of $T'$-$MoS_2$. For S atoms, we divide them into two groups [labeled by $S_1$ (orange) and $S_2$ (yellow)], where two atoms in each group are connected by inversion symmetry. The green line in (a) represents the reflected mirror $\sigma_h(yz)$. (c) Brillouin zone of monolayer $T'$-$MoS_2$. Other $T'$-$MX_2$ materials possess the same lattice structures with different lattice constants. The band gap is located around the red dots shown in (c).

at $-\Lambda(+\Lambda)$ as shown in Fig. 2(b). Since the monolayer $T'$-$MoS_2$ has both time-reversal and space-inversion symmetry, the band structure shown in Figs. 2(a) and 2(b) is strictly degenerate for different spin in the absence of the PEF. However, the PEF can break the space-inversion symmetry and give rise to a spin-splitting band structure shown in Fig. 2(c1). As the PEF strength increases, the band gap first decreases to zero at a critical field strength of $E_c = 7.36$ MV/cm and then reopens

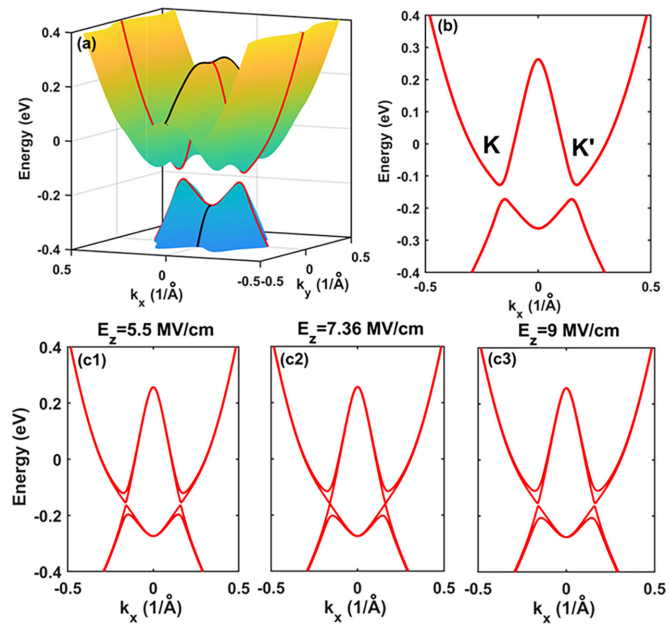


FIG. 2. Calculated electronic structures of $T'$-$MoS_2$ using DFT. (a) Band structure with SOC and (b) band structure along $-X \leftarrow \Gamma \rightarrow X$ path ($k_y = 0$). Here we define the $K$ and $K'$ valley located around red dots shown in Fig. 1(c). DFT results for monolayer $1T'$-$MoS_2$ under perpendicular electric fields of (c1) $E_z = 5.5$, (c2) $E_z = 7.36$, and (c3) $E_z = 9$ MV/cm, respectively.

as shown in Figs. 2(c2) and 2(c3). This gap-closing transition induces a topology change to a trivial phase.

In order to describe the PEF effect on band structure and spin properties, we construct a $4\times4$ $\mathbf{k}\cdot\mathbf{p}$ Hamiltonian using both group theory [21,22] and the tight-binding method [23] respectively. The detailed process of the Hamiltonian construction can be found in the Appendix. Here we directly display the $\mathbf{k}\cdot\mathbf{p}$ Hamiltonian:

$$\mathbf{H}_{\mathbf{k}\cdot\mathbf{p}}=\begin{bmatrix} E_{11} & 0 & w_1E_z+c_4k_x+ic_1k_y & iw_2E_z-ic_3k_x+c_2k_y \\ & E_{22} & iw_2E_z+ic_3k_x+c_2k_y & w_1E_z-c_4k_x+ic_1k_y \\ & & E_{33} & 0 \\ & & & E_{44} \end{bmatrix},$$

$$E_{11}=\delta+v_1k_x^2+v_2k_y^2+f_1E_zk_x,\quad E_{22}=\delta+v_1k_x^2+v_2k_y^2-f_1E_zk_x,$$
$$E_{33}=-\delta+v_3k_x^2+v_4k_y^2+f_2E_zk_x,\quad E_{44}=-\delta+v_3k_x^2+v_4k_y^2-f_2E_zk_x. \tag{1}$$

In Eq. (1) we keep only the lowest-order contribution to each matrix element, and give only the matrix elements in the upper triangle since the $\mathbf{k}\cdot\mathbf{p}$ Hamiltonian is Hermitian. All the parameters in the $\mathbf{k}\cdot\mathbf{p}$ Hamiltonian are listed in Table I.

The comparison between the results obtained using the $\mathbf{k}\cdot\mathbf{p}$ Hamiltonian and the first-principles calculations are shown in Fig. 3. Even though all the figures in Fig. 3 display the results for monolayer $T'$-$MoS_2$ under the specific electric field of $E_z=7$ MV/cm, the Hamiltonian in Eq. (1) can also be used to describe the electronic dispersion and spin texture under different electric fields ($E_z$). As we can see in Figs. 3(a1) and 3(a2), our $\mathbf{k}\cdot\mathbf{p}$ Hamiltonian captures the nonparabolic dispersion, which is an interesting feature of the monolayer $T'$-$MoS_2$ that may exhibit unconventional transport properties. It is worth noting that the PEF splits the band structure in Figs. 3(a1) and 3(a2) into four bands marked with different colors: green, black, red, and blue. Fortunately, the spin projection ($\langle s_\xi\rangle$, $\xi=x,y,z$) obtained using our $\mathbf{k}\cdot\mathbf{p}$ Hamiltonian [shown in Figs. 3(b1)–3(d1)] is in agreement with the results obtained using first-principles calculation [shown in Figs. 3(b2)–3(d2)]. Here the spin projection ($\langle s_\xi\rangle$, $\xi=x,y,z$) stands for the expectation value of spin for a specific Bloch state ($\langle s_\xi\rangle=\langle\psi_n(k_x,k_y)|s_\xi|\psi_n(k_x,k_y)\rangle$), where $n$ represents the band index. In physical view, we can determine whether there is nonzero spin polarization or not by summing up the spin projection ($\langle s_\xi\rangle$) for all the Bloch states located at the Fermi circle. Therefore it is essential to calculate and analyze the spin projection in $k$ space.

As we can see in Fig. 3, the spin projection $\langle s_y\rangle$ and $\langle s_z\rangle$ have values and exhibit odd parity properties along

TABLE I. Nonzero $\mathbf{k}\cdot\mathbf{p}$ parameters in the monolayer $T'$-$MX_2$ ($MX_2$ = $MoS_2$, $WSe_2$, and $WS_2$) $\mathbf{k}\cdot\mathbf{p}$ Hamiltonian.

| Parameter | $MoS_2$ | $WSe_2$ | $WS_2$ | Unit |
|---|---|---|---|---|
| $\delta$ | 0.2631 | 0.3388 | 0.0897 | eV |
| $v_1$ | −9.0503 | −58.5032 | −12.5025 | eV Å$^2$ |
| $v_2$ | −1.8201 | −0.8201 | −1.8201 | eV Å$^2$ |
| $v_3$ | 2.3284 | 2.2447 | 1.3501 | eV Å$^2$ |
| $v_4$ | −0.2109 | −0.5109 | −0.2109 | eV Å$^2$ |
| $c_1$ | −1.4025 | −1.5021 | −1.4025 | eV Å |
| $c_2$ | 0.6756 | −1.0913 | 0.6756 | eV Å |
| $c_3$ | −0.1763 | −0.7304 | 0.6716 | eV Å |
| $c_4$ | −0.0661 | −0.2738 | 0.1974 | eVÅ |
| $w_1$ | −0.5494 | −0.5759 | 0.4043 | e Å |
| $w_2$ | −0.0346 | −0.1871 | 0.0682 | e Å |
| $f_1$ | −0.3403 | −1.3698 | −0.2469 | e Å$^2$ |
| $f_2$ | 0.0902 | 0.2171 | −0.0391 | e Å$^2$ |

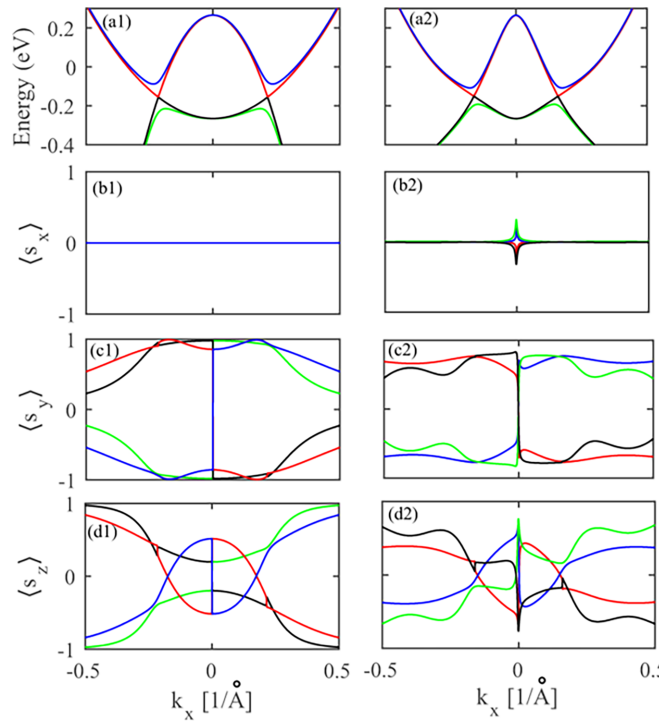


FIG. 3. Comparison of band structure and spin texture results along the $-X\leftarrow\Gamma\rightarrow X$ direction ($k_y=0$/Å) calculated using $\mathbf{k}\cdot\mathbf{p}$ Hamiltonian shown in Eq. (1) and DFT. (a1) and (a2) are band structure obtained from the $\mathbf{k}\cdot\mathbf{p}$ Hamiltonian and the first-principles calculations. The solid lines of different colors (blue, red, black, and green) in (b1), (c1), and (d1), respectively correspond to the spin projection $\langle s_x\rangle$, $\langle s_y\rangle$, and $\langle s_z\rangle$ of different energy bands in (a1). The solid lines of different colors (blue, red, black, and green) in (b2), (c2), and (d2), respectively, correspond to the spin projection $\langle s_x\rangle$, $\langle s_y\rangle$, and $\langle s_z\rangle$ of different energy bands in (a2). All these figures are results for monolayer $T'$-$MoS_2$ under specific electric field strength $E_z=7$ MV/cm.

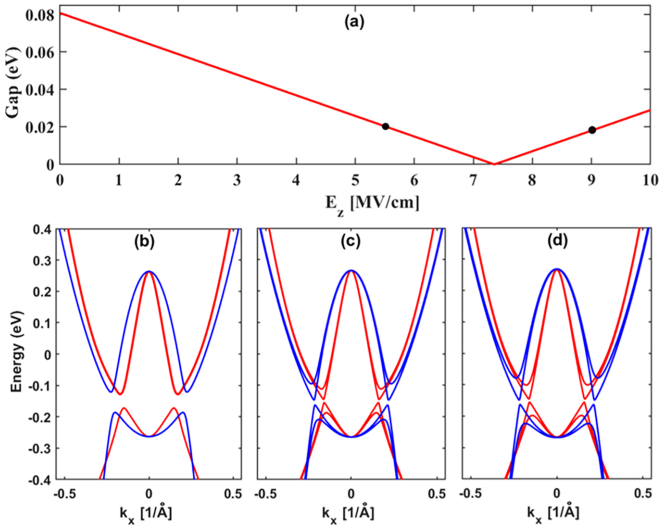


FIG. 4. (a) Band gap of $T'$-$MoS_2$ as a function of perpendicular electric field (PEF). The two black dots indicate the situations when the PEF strength is 5.5 and 9 MV/cm, respectively. (b)–(d) Band structure of monolayer $T'$-$MoS_2$ under different perpendicular electric strength: (b) $E_z = 0$, (c) $E_z = 5.5$, and (d) $E_z = 9$ MV/cm, calculated using our $\mathbf{k}\cdot\mathbf{p}$ model Hamiltonian (blue lines) and first-principles calculations (red lines).

the $k_x(k_y = 0)$ direction, while the spin projection $\langle s_x\rangle$ is zero along the $k_x(k_y = 0)$ direction. This phenomenon can be explained by symmetry analysis. Since the spin operator component $s_y$ is odd with respect to time reversal and mirror reflection $\sigma_h(yz)$, invariance under time reversal and mirror reflection $\sigma_h(yz)$ imposes only one condition on the spin projection: $\langle\psi_n(-k_x,0)|s_y|\psi_n(-k_x,0)\rangle = -\langle\psi_n(k_x,0)|s_y|\psi_n(k_x,0)\rangle$ (where $n$ stands for the band index). Therefore, the spin projection $\langle s_y\rangle$ exhibits odd parity properties along the $k_x(k_y = 0)$ direction. The same analysis can lead to the conclusion that $\langle s_z\rangle$ also exhibits odd parity properties.

However, the situation is different for spin projection $\langle s_x\rangle$. On one hand, the spin operator component $s_x$ is odd with respect to time reversal, and invariance under time reversal imposes a condition on the spin projection: $\langle\psi_n(-k_x,0)|s_x|\psi_n(-k_x,0)\rangle = -\langle\psi_n(k_x,0)|s_x|\psi_n(k_x,0)\rangle$. On the other hand, the spin operator component $s_x$ is even with respect to mirror reflection $\sigma_h(yz)$, and invariance under mirror reflection $\sigma_h(yz)$ imposes another condition on the spin projection: $\langle\psi_n(-k_x,0)|s_x|\psi_n(-k_x,0)\rangle = \langle\psi_n(k_x,0)|s_x|\psi_n(k_x,0)\rangle$. The spin projection $\langle s_x\rangle$ along the $k_x$ direction that satisfies both of the above two conditions can only be zero, as shown in Fig. 3(b1).

Although, we treat PEF $E_z$ as a perturbation in the above deduction, the $\mathbf{k}\cdot\mathbf{p}$ Hamiltonian still can be used to predict the phase transition induced by large $E_z$. As we can see in Fig. 4(a), when the PEF $E_z$ increases from zero to significantly large, the band gap ($E_g$) closes and reopens. The phase transition under the PEF $E_z$ obtained using our model is in good agreement with the result predicted using first-principles calculation. Under different PEF strength, the band structure calculated using our $\mathbf{k}\cdot\mathbf{p}$ model [blue lines in Figs. 4(b)–4(d)] is in agreement with the DFT results [red lines in Figs. 4(b)–4(d)].

## III. CURRENT-INDUCED SPIN POLARIZATION

The current-induced spin polarization (CISP), also known as the Edelstein effect or the charge-to-spin conversion, is that a charge current driven through a 2D system with Rashba spin-orbit coupling (RSOC) generates a spatially homogeneous spin polarization perpendicular to the applied bias [24,25]. Thus a nonzero spin polarization is generated in nonmagnetic systems purely electrically. The PEF that gives rise to the RSOC effect is responsible for CISP taking place in monolayer $T'$-$MoS_2$, where the RSOC can be tuned by gate voltages. At low temperature, the CISP response is determined by the spin texture near the Fermi surface, which can be well described using our $\mathbf{k}\cdot\mathbf{p}$ Hamiltonian [Eq. (1)].

According to the Onsager relation, the charge-to-spin conductivity (C-S conductivity) is equal to the spin-to-charge conductivity, which reads [26,27]

$$\langle J_\alpha; S_\beta\rangle = -\frac{e}{2\pi}\int\frac{d^2p}{(2\pi)^2}\mathbf{Tr}[J_\alpha G^R(\mu)S_\beta G^A(\mu)], \quad (2)$$

where $J_\alpha = ev_\alpha = e\partial\mathbf{H}_{\mathbf{k}\cdot\mathbf{p}}/\partial k_\alpha(\alpha = x, y)$ is the current operator, $S_\beta$ is the spin operator, and $G^{R(A)}$ is the retarded (advanced) Green function corresponding to the unperturbed Hamiltonian $\mathbf{H}_{\mathbf{k}\cdot\mathbf{p}}$, taken at the chemical potential $\mu$. For the clean-limit situation, the C-S conductivity ($\langle J_\alpha; S_\beta\rangle$) could become divergent. This would not happen in real materials, where the impurity scattering causes a finite lifetime of the carriers.

Here we calculate the C-S conductivity with disorder effects taken into consideration. For a disordered system, $G^{R(A)}$ in Eq. (2) should be understood as disorder-averaged Green's functions:

$$G^{R(A)} = \frac{1}{\mu - \mathbf{H}_{\mathbf{k}\cdot\mathbf{p}} \pm i\Gamma}, \quad (3)$$

where $\Gamma = \hbar/(2\tau)$ is the level broadening due to the disorder. For randomly distributed short-range impurities described by a random potential $V(r)$ with Gaussian correlation $\langle V(r)V(r')\rangle = n_i v_0^2\delta(r - r')$, we can use the Born approximation to obtain $\Gamma = n_i v_0^2 N(\mu)$, where $n_i$ is the impurity density, $v_0$ is the disorder scattering potential, and $N(\mu)$ is the density of states (DOS) at the chemical potential $\mu$.

Using Eq. (2), we calculate the zero-temperature C-S conductivity vs chemical potential $\mu$ under different PEF for different disorder strength and plot the results in Figs. 5(b) and 5(d). The corresponding band structure is shown in Figs. 5(a) and 5(c). Although there is a topological phase transition when the PEF increases from zero to 10 MV/cm (shown in Fig. 4), the charge-to-spin response follows same mode, as shown in Figs. 5(b) and 5(d). Since the in-plane charge-to-spin response is much smaller than the out-of-plane response, we show only the C-S conductivity of $\langle J_x; S_z\rangle$. It is worth noting that the out-of-plane spin polarization $S_z$ induced by the current along the $y$ direction is forbidden ($\langle J_y; S_z\rangle = 0$). These anisotropic phenomena can be explained by analyzing spin texture shown in Fig. 6.

Figure 6 shows the spin texture on the Fermi surface of the $T'$-$MoS_2$ monolayer under PEF ($E_z = 5.5$ MV/cm) with the Fermi level located at $\mu = -0.12$ eV. As we can see, the blue (red) circles stand for the Fermi surface without (with)

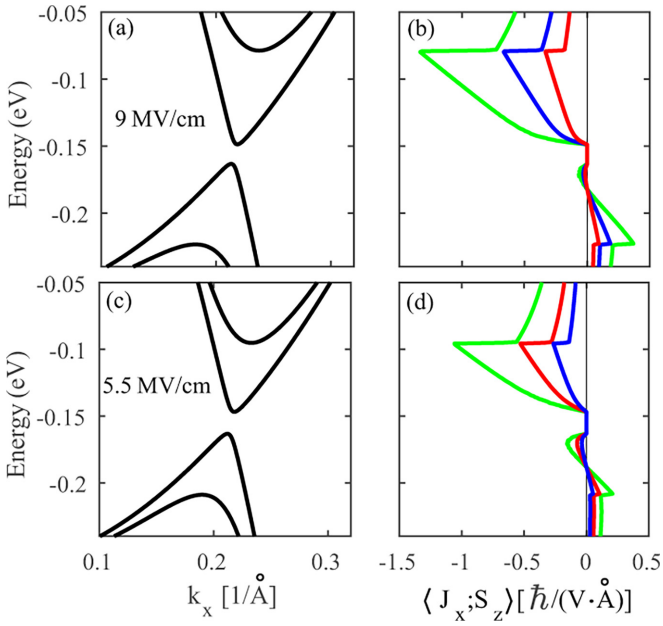


FIG. 5. (a), (c) Band structure of $T'$-$MoS_2$ monolayer calculated using the multiband $\mathbf{k}\cdot\mathbf{p}$ model under different PEF: (a) $E_z = 9$ MV/cm, (c) $E_z = 5.5$ MV/cm. (b), (d) Corresponding charge-spin conductivity $\langle J_x; S_z\rangle$ calculated using the multiband $\mathbf{k}\cdot\mathbf{p}$ model under different PEF, and for different disorder strengths $n_i v_0^2 = 0.8 \times 10^{-2}$ (eV Å)$^2$ (green lines), $n_i v_0^2 = 1.6 \times 10^{-2}$ (eV Å)$^2$ (red lines), and $n_i v_0^2 = 3.2 \times 10^{-2}$ (eVÅ)$^2$ (blue lines).

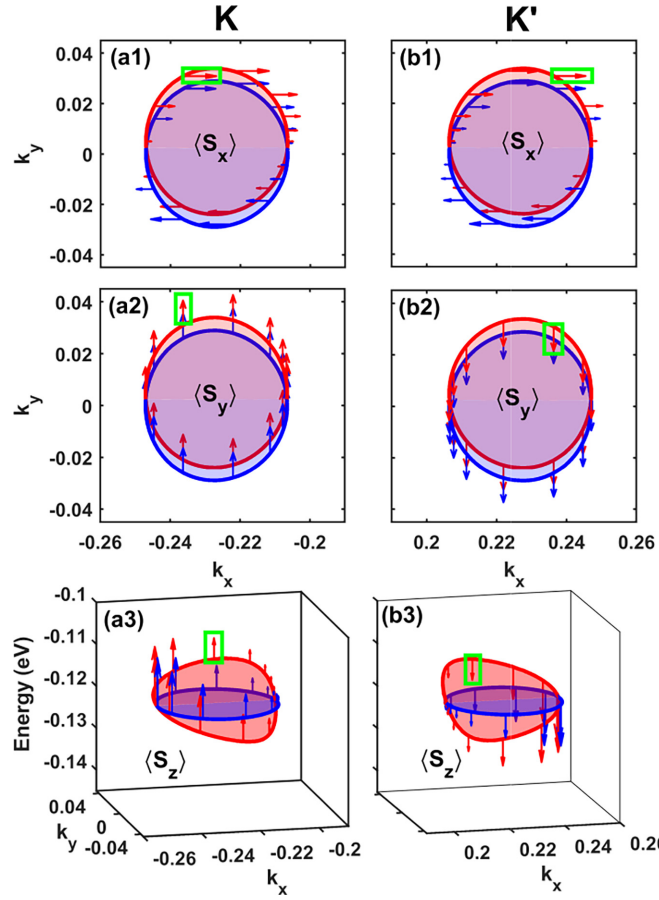


FIG. 6. (a1) [(b1)], (a2) [(b2)], and (a3) [(b3)] are the $\langle s_x\rangle$, $\langle s_y\rangle$, and $\langle s_z\rangle$ projected spin texture, respectively, at Fermi level $\mu = -0.12$ eV near the $K$ ($K'$) valley. In all these figures the blue (red) circle represents the Fermi surface without (with) bias voltage along the $y$ direction. The PEF along the $z$ direction is $E_z = 5.5$ MV/cm, which corresponds to the results shown in Fig. 2(c1).

bias along the $y$ direction. The blue (red) arrows at the Fermi circle represent the spin momentum (namely, spin texture: $\langle s_x\rangle$, $\langle s_y\rangle$, and $\langle s_z\rangle$) of the occupation states at the Fermi circle. Physically, the spin polarization can be considered as the summation of all the spin momentum at the red Fermi circles. Without in-plane bias voltage, the summation of all the spin momentum at the blue Fermi circles in the $K$ [Fig. 6(a1)] and $K'$ [Fig. 6(b1)] valley is zero, which indicates that there is no $S_x$ spin polarization. It is obvious that without in-plane bias voltage, there is no $S_y$ and $S_z$ spin polarization too.

When there is a bias voltage along the $y$ direction, the electron occupation states are redistributed [28,29], and the Fermi surface drifts from the blue circles to the red circles shown in Fig. 6. Since the $T'$-$MoS_2$ monolayer has mirror symmetry (the reflected mirror is the $yz$ plane), the specific spin momentum in the $K$ valley [red arrow in green box shown in Fig. 6(a3)] and the spin momentum in the $K'$ valley [red arrow in green box shown in Fig. 6(b3)] have identical values with opposite directions. Therefore, the $y$ direction charge current cannot induce a spin polarization along the $z$ direction ($\langle J_y; S_z\rangle = 0$). It is obvious that the $y$ direction current cannot induce the spin polarization $S_y$ too ($\langle J_y; S_y\rangle = 0$).

However, the transform of spin momentum $s_x$ under mirror reflection [$\sigma_h(yz)$] is different from the spin momentum $s_y$ or $s_z$, which gives rise to an identical direction between the spin momentum in the $K$ and $K'$ valleys [as shown in Figs. 6(a1) and 6(b1), the red arrows in green box have identical value and point in the same direction]. Therefore, the $y$ direction charge current can induce the spin polarization only along the $x$ direction ($\langle J_y; S_x\rangle \neq 0$).

As we can see in Fig. 7, the bias voltage along the $x$ direction leads to the electron occupation states redistribution, and the Fermi surface drifts to the red circles. It is worth noting that the summation of the $x$ direction projected spin texture $\langle s_x\rangle$ at blue (red) Fermi circles shown in Figs. 7(a1) and 7(b1) equals zero. In other words, there is no $x$ direction spin polarization induced by the charge current along the $x$ direction. The vanish of the spin polarization $S_x$ can be understood by analyzing the spin texture shown in Fig. 7(a1). Since the system has both time-reversal invariance and mirror symmetry ($\sigma_h(yz)$), the spin momentum in the small green box in Fig. 7(a1) has an identical value with an opposite direction compared with the spin momentum in the small black box. Therefore, the current ($x$ direction) induced spin polarization $S_x$ is forbidden $\langle J_x; S_x\rangle = 0$.

We conclude that the symmetry-allowed charge-to-spin response is $\langle J_x; S_y\rangle$, $\langle J_y; S_x\rangle$ and $\langle J_x; S_z\rangle$. Although the existance of charge-to-spin response is decided by the crystal symmetry, the strength of the response depends on the change of spin texture induced by the Fermi surface drifting. According to our calculation, the in-plane charge-to-spin response $\langle J_x; S_y\rangle$, $\langle J_y; S_x\rangle$ is much smaller than the out-of-plane response $\langle J_x; S_z\rangle$.

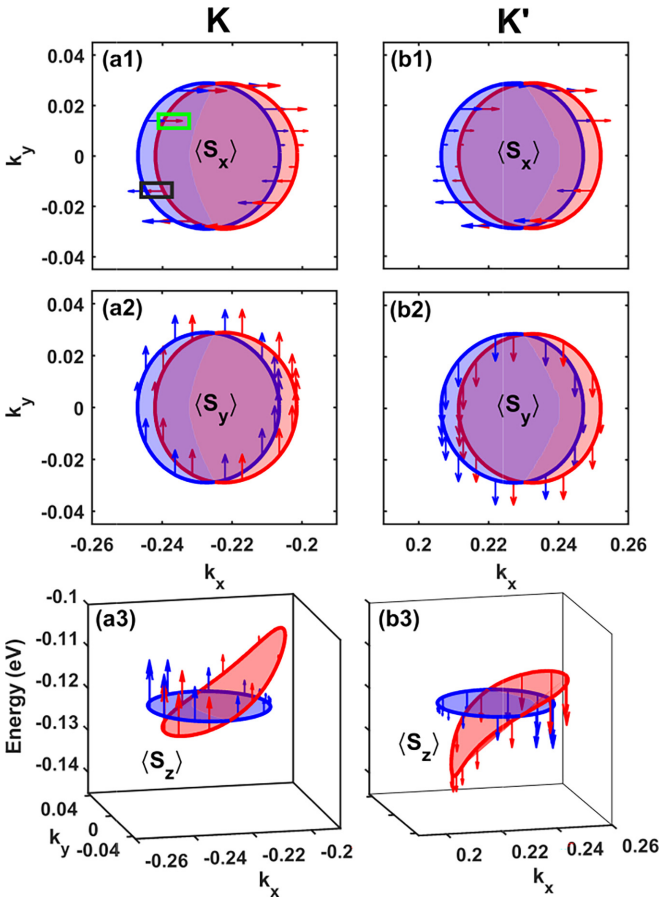


FIG. 7. (a1) [(b1)], (a2) [(b2)], and (a3) [(b3)] are the $\langle s_x\rangle$, $\langle s_y\rangle$, and $\langle s_z\rangle$ projected spin texture, respectively, at the Fermi level $\mu = -0.12$ eV near the $K$ ($K'$) valley. In all these figures the blue (red) circle represents the Fermi surface without (with) bias voltage along the $x$ direction. The PEF along the $z$ direction is $E_z = 5.5$ MV/cm, which corresponds to the results shown in Fig. 2(c1).

## IV. CONCLUSION

We obtain the effective $\mathbf{k}\cdot\mathbf{p}$ Hamiltonian for an electron in monolayer $T'$-$MoS_2$ near the Fermi level in the presence of spin-orbit coupling and a perpendicular electric field. The $4\times 4$ $\mathbf{k}\cdot\mathbf{p}$ Hamiltonian can describe the band dispersion and perpendicular electric field-induced spin texture very well. By using the $\mathbf{k}\cdot\mathbf{p}$ Hamiltonian, we predict a significantly large out-of-plane spin polarization ($S_z$) induced by the charge current along the $x$ direction. Furthermore, we find that the mirror symmetry [$\sigma_h(yz)$] leads to the forbidden spin polarization ($S_z$) induced by the charge current along the $y$ direction.

## APPENDIX

### 1. Group theory

Here we derive the effective $\mathbf{k}\cdot\mathbf{p}$ Hamiltonian using group theory. As shown in Fig. 1, the monolayer $T'$-$MoS_2$ has a rectangular unit cell (red-shaded area) with two Mo atoms and four S atoms. The monolayer $T'$-$MoS_2$ belongs to a nonsymmorphic space group, containing the following symmetries: (1) glide mirror $T(\frac{R_x}{2})\sigma_h$: $(x, y, z) \to (-x, y, z) + \frac{R_x}{2}$ and (2) screw rotation $T(\frac{R_x}{2})C_2$: $(x, y, z) \to (x, -y, -z) + \frac{R_x}{2}$. Here the glide mirror operation can be divided into two symmetry operations: $yz$ plane mirror reflection $\sigma_h$ [the reflective plane is indicated by the green line in Fig. 1(a)] and translation $\frac{R_x}{2}$ along the $x$ direction. The screw rotation is composed of a 180° rotation along the $x$ axes within the translation $\frac{R_x}{2}$ along the $x$ direction. Although the space group of monolayer $T'$-$MoS_2$ is nonsymmorphic, we can construct the effective $\mathbf{k}\cdot\mathbf{p}$ Hamiltonian in the basis of the Bloch function at the Γ point using the $C_{2h}$ point group. Table II shows the character table for $C_{2h}$ point group. The $C_{2h}$ point group consists of four symmetry operations divided into four classes and hence four irreducible representations (see Table II).

TABLE II. Character table of point group $C_{2h}$ and the tensor components for each irreducible representation. Here $(k_x, k_y)$ are the three Cartesian components of an wave vector (that changes sign under spatial inversion), and $(s_x, s_y, s_z)$ are the three Cartesian components of spin. $E_z$ stands for perpendicular electric field.

| | E | $C_2$ | I | $\sigma_h$ | Tensor components |
|---|---|---|---|---|---|
| $\Gamma_1^+$ | 1 | 1 | 1 | 1 | $\{s_x\}$, $\{k_x^2\}$, $\{k_y^2\}$, $\{E_z k_y\}$ |
| $\Gamma_2^+$ | 1 | −1 | 1 | −1 | $\{s_y\}$, $\{s_z\}$, $\{k_x k_y\}$, $\{E_z k_x\}$ |
| $\Gamma_1^-$ | 1 | 1 | −1 | −1 | $\{k_x\}$, $\{k_x s_x\}$, $\{k_y s_y\}$, $\{E_z s_y\}$, $\{k_y s_z\}$, $\{E_z s_z\}$ |
| $\Gamma_2^-$ | 1 | −1 | −1 | 1 | $\{k_y\}$, $\{E_z\}$, $\{k_y s_x\}$, $\{E_z s_x\}$, $\{k_x s_y\}$, $\{k_x s_z\}$ |

As we can see in Fig. 8, in the absence of spin-orbit coupling (SOC), the electronic properties of monolayer $T'$-$MoS_2$ are dominated by two energy bands in the vicinity of the Fermi level. Their orbital wave functions at the Γ point are $|\psi_c\rangle$ and $|\psi_v\rangle$, which consist of the $p_x$ orbital of S atoms [shown in Fig. 8(a)] and $d$ orbitals of Mo atoms [shown in Figs. 8(b) and 8(c)]. Although there are two different possible configurations (bonding or antibonding configuration) of the $p_x$ orbitals within a unit cell, all the configurations are odd under the glide mirror operator $T(\frac{R_x}{2})\sigma_h$. Therefore, the orbital wave functions $|\psi_c\rangle$ and $|\psi_v\rangle$ belong to $\Gamma_1^-$ or $\Gamma_2^+$ irreducible representation (IR) of the $C_{2h}$ point group.

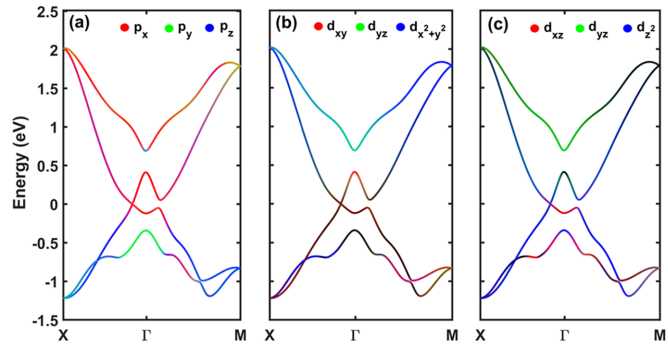


FIG. 8. Orbital projections for monolayer $T'$-$MoS_2$ from first-principles calculations. The color represents the weight of a specific orbital. (a) The projection results from $p$ orbitals of S atom, red for $p_x$, green for $p_y$, and blue for $p_z$. (b) The result of contributions from $d$ orbitals of Mo atoms, red for $d_{xy}$, green for $d_{yz}$, and blue for $d_{x^2+y^2}$. (c) The result of contributions from $d$ orbitals of Mo atoms, red for $d_{xz}$, green for $d_{yz}$, and blue for $d_{z^2}$.

Furthermore, it is worth noting that the band structure crosses over along the $\Gamma \to X$ direction. This crossover implies that the wave functions $|\psi_c\rangle$ and $|\psi_v\rangle$ belong to different IR, otherwise the band structure along the $\Gamma \to X$ direction will open a gap due to the $k_x^2$ term, which belongs to $\Gamma_1$ IR. According to the analyses above, we conclude that there are only two possible cases: (1) $|\psi_c\rangle$ ($|\psi_v\rangle$) belongs to $\Gamma_1^-$ ($\Gamma_2^+$) IR and (2) $|\psi_c\rangle$ ($|\psi_v\rangle$) belongs to $\Gamma_2^+$ ($\Gamma_1^-$) IR. In either case we will obtain the same model Hamiltonian.

In the basis $\{|\psi_c\rangle, |\psi_v\rangle\}$, the $\mathbf{k}\cdot\mathbf{p}$ Hamiltonian assumes the $2\times 2$ block form:

$$\mathbf{H} = \begin{bmatrix} \mathbf{H}^{c,c} & \mathbf{H}^{c,v} \\ \mathbf{H}^{v,c} & \mathbf{H}^{v,v} \end{bmatrix}, \tag{A1}$$

where $\mathbf{H}^{\alpha,\beta}$ is the matrix element between $|\psi_\alpha\rangle$ and $|\psi_\beta\rangle$, e.g., $\mathbf{H}^{c,v} = \langle\psi_c|H|\psi_v\rangle$. According to the theory of invariants, all the matrix block ($\langle\psi_\alpha|H|\psi_\beta\rangle$) should satisfy two conditions:

(1) The transform of the matrix block under all the symmetry operations of $C_{2h}$ point group should be invariant.

(2) In addition to the point group symmetry, the $\mathbf{k}\cdot\mathbf{p}$ Hamiltonian must obey the time-reversal symmetry.

In order to satisfy condition (1), every term in Hamiltonian block $\mathbf{H}^{\alpha,\beta}$ must transform like $\Gamma_\gamma$, where $\Gamma_\gamma = \Gamma_\alpha \otimes \Gamma_\beta$. Combining the additional conditions imposed on Hamiltonian by time-reversal symmetry, we can easily obtain the symmetry-allowed Hamiltonian block as follows:

$$\begin{aligned} \mathbf{H}^{cc} &= \{k_x^2\} + \{k_y^2\} + \{E_z k_x s_z\}, \\ \mathbf{H}^{cv} &= \{ik_y\} + \{k_y s_x\} + \{k_x s_y\} + \{k_x s_z\} + \{E_z\} + \{iE_z s_x\}. \end{aligned} \tag{A2}$$

Here the braces remind us there is an undetermined coefficient before each term which can be numerically fitted out. It is worth noting that the Hamiltonian block $\mathbf{H}^{vv}$ shares the same form with the $\mathbf{H}^{cc}$, but the coefficients are different. Substituting the $s_x, s_y, s_z$ with the Pauli matrix, we obtain the form of the effective $\mathbf{k}\cdot\mathbf{p}$ Hamiltonian shown in Eq. (1).

Altogether there are 12 real parameters, including band-edge energy $\delta$, eight coefficients $c_1, c_2, c_3, c_4, v_1, v_2, v_3, v_4$ associated with the $k$-dependent matrix elements, two coefficients $w_1, w_2$ associated with the $E_z$ matrix elements, and two coefficients $f_1, f_2$ that describe the coupling between $E_z$ and wave vector $k_x$. All these parameters can be determined by comparing the energy band structure obtained from the $\mathbf{k}\cdot\mathbf{p}$ Hamiltonian [Eq. (1)] to the first-principles calculations in the vicinity of the $\Gamma$ point. The fitting results of parameters are listed in Table. 1.

### 2. Tight binding

As we can see in Fig. 8(a), the states in the energy window ([−0.2 eV, 0.5 eV]) are mostly contributed by the $p_x$ orbital of an S atom. According to results shown in Figs. 8(b) and 8(c), the states near the Fermi level are mainly composed of $d_{xy}$ and $d_{xz}$ orbitals of an Mo atom. Here we construct a tight-binding Hamiltonian in the Hilbert space constituted by four orbitals $\{p_x, d_{xy}, d_{xz}, d_{x^2+y^2}\}$ to describe the electronic structure near the Fermi energy level. Since there are two Mo atoms (Mo in A and B) and two $S_1$ atoms ($S_1$ in A and B) in the unit cell shown in Fig. 1 red-shaded area, we write the $8\times 8$ tight-binding matrix in the basis $\{|d^A_{x^2-y^2}\rangle, |d^B_{x^2-y^2}\rangle, |d^A_{zx}\rangle, |p^A_x\rangle, |d^B_{zx}\rangle, |p^B_x\rangle, |d^A_{xy}\rangle, |d^B_{xy}\rangle\}$ as follows:

$$\mathbf{H_{TB}} = \begin{bmatrix} h_{11} & h_{12} & 0 & 0 & 0 & h_{16} & 0 & h_{18} \\ & h_{22} & 0 & h_{24} & 0 & 0 & h_{27} & 0 \\ & & h_{33} & h_{34} & h_{35} & h_{36} & 0 & 0 \\ & & & h_{44} & h_{45} & h_{46} & h_{47} & h_{48} \\ & & & & h_{55} & h_{56} & 0 & 0 \\ & & & & & h_{66} & h_{67} & h_{68} \\ & & & & & & h_{77} & h_{78} \\ & & & & & & & h_{88} \end{bmatrix},$$

$$h_{11} = h_{22} = \mu_d + 2t_{d1}\cos(R_x k_x), \quad h_{33} = h_{55} = \mu_d + 2t_{d2}\cos(R_x k_x),$$

$$h_{44} = h_{66} = \mu_p + 2t_p\cos(R_x k_x), \quad h_{77} = h_{88} = \mu_d + 2t_{d3}\cos(R_x k_x),$$

$$h_{12} = 2t_1 e^{ik_y d_{1y}}\cos\left(\frac{R_x k_x}{2}\right); \quad h_{16} = 2it_2 e^{ik_y d_{2y}}\sin\left(\frac{R_x k_x}{2}\right),$$

$$h_{18} = 2it_6 e^{ik_y d_{1y}}\sin\left(\frac{R_x k_x}{2}\right); \quad h_{24} = 2it_2 e^{-ik_y d_{2y}}\sin\left(\frac{R_x k_x}{2}\right),$$

$$h_{27} = -2it_6 e^{-ik_y d_{1y}}\sin\left(\frac{R_x k_x}{2}\right); \quad h_{34} = t_z e^{-ik_y d_{0y}},$$

$$h_{35} = 2t_4 e^{ik_y d_{1y}}\cos\left(\frac{R_x k_x}{2}\right); \quad h_{36} = 2t_3 e^{ik_y d_{2y}}\cos\left(\frac{R_x k_x}{2}\right),$$

$$h_{45} = -2t_3 e^{ik_y d_{2y}}\cos\left(\frac{R_x k_x}{2}\right); \quad h_{46} = 2t_5 e^{-ik_y d_{3y}}\cos\left(\frac{R_x k_x}{2}\right),$$

$$h_{47} = t_7 e^{ik_y d_{0y}}; \quad h_{48} = 2t_8 e^{ik_y d_{2y}} \cos\left(\frac{R_x k_x}{2}\right),$$
$$h_{56} = -t_z e^{ik_y d_{0y}}; \quad h_{67} = -2t_8 e^{-ik_y d_{2y}} \cos\left(\frac{R_x k_x}{2}\right),$$
$$h_{68} = -t_7 e^{-ik_y d_{0y}}; \quad h_{78} = 2t_9 e^{ik_y d_{1y}} \cos\left(\frac{R_x k_x}{2}\right). \tag{A3}$$

Here $\mathbf{d_0}$, $\mathbf{d_1}$, $\mathbf{d_2}$, $\mathbf{d_3}$ and $R_x$, $R_y$ are vectors shown in Fig. 1. In the above we give only the matrix elements in the upper triangle since the tight-binding Hamiltonian is Hermitian.

Around the Γ point, the tight-binding Hamiltonian can be decomposed into two parts. The first part is the Γ point Hamiltonian $\mathbf{H_0}$ (where $k_x = k_y = 0$):

$$\mathbf{H_0} = \mathrm{diag}[\mu_d + 2t_{d1}, \mu_d + 2t_{d1}, \mu_d + 2t_{d2}, \mu_p + 2t_p, \mu_d + 2t_{d2}, \mu_p + 2t_p, \mu_d + 2t_{d3}, \mu_d + 2t_{d3}]$$
$$+ \begin{bmatrix} 0 & 2t_1 & 0 & 0 & 0 & 0 & 0 & 0 \\ & 0 & 0 & 0 & 0 & 0 & 0 & 0 \\ & & 0 & t_z & 2t_4 & 2t_3 & 0 & 0 \\ & & & 0 & -2t_3 & 2t_5 & t_7 & 2t_8 \\ & & & & 0 & -t_z & 0 & 0 \\ & & & & & 0 & -2t_8 & -t_7 \\ & & & & & & 0 & 2t_9 \\ & & & & & & & 0 \end{bmatrix}. \tag{A4}$$

The second part is the perturbation part $\mathbf{H_k} = \begin{bmatrix} H_{11} & H_{12} \\ H_{21} & H_{22} \end{bmatrix}$. The matrix element $H_{11}$, $H_{12}$, $H_{21}$, $H_{22}$ has the following form:

$$H_{11} = \begin{bmatrix} 0 & 2it_1 d_{1y} k_y \\ & 0 \end{bmatrix}, \tag{A5}$$

$$H_{12} = H_{21}^{\dagger} = \begin{bmatrix} 0 & 0 & 0 & it_2 R_x k_x & 0 & it_6 R_x k_x \\ 0 & it_2 R_x k_x & 0 & 0 & -it_6 R_x k_x & 0 \end{bmatrix},$$

$$H_{22} = \begin{bmatrix} 0 & -it_z d_{0y} k_y & 2it_4 d_{1y} k_y & 2it_3 d_{2y} k_y & 0 & 0 \\ & 0 & -2it_3 d_{2y} k_y & -2it_5 d_{3y} k_y & it_7 d_{0y} k_y & -it_8 R_x k_x \\ & & 0 & -it_z d_{0y} k_y & 0 & 0 \\ & & & 0 & it_8 R_x k_x & it_7 d_{0y} k_y \\ & & & & 0 & it_9 d_{1y} k_y \\ & & & & & 0 \end{bmatrix}, \tag{A6}$$

where $k_x$, $k_y$ has a small value.

We can also treat spin-orbital coupling and the perpendicular electric field as small perturbations. In above atomic orbital space, the SOC Hamiltonian $H_{so}$ and PEF Hamiltonian $H_{Ez}$ can be written as

$$H_{so} + H_{E_z} = \begin{bmatrix} 0 & 0 & i\lambda_d s_y & 0 & 0 & 0 & -2i\lambda_d s_z & 0 \\ & 0 & 0 & 0 & i\lambda_d s_y & 0 & 0 & -2i\lambda_d s_z \\ & & 0 & 0 & 0 & 0 & i\lambda_d s_x & 0 \\ & & & E_z & 0 & 0 & 0 & 0 \\ & & & & 0 & 0 & 0 & i\lambda_d s_x \\ & & & & & -E_z & 0 & 0 \\ & & & & & & 0 & 0 \\ & & & & & & & 0 \end{bmatrix}, \tag{A7}$$

where $\lambda_d$ is the $d$ orbital SOC strength of the Mo atom, and the Pauli matrix $s_x$, $s_y$, $s_z$ is acting on the spin subspace. $E_z$ represents the PEF-induced potential difference between the S atom in the A and B sublattice shown in Fig. 1.

By transforming the atom basis perturbation Hamiltonian $H_k + H_{so} + H_{E_z}$ into the Γ point Bloch basis, which can be obtained by diagonalizing the Γ point Hamiltonian $H_0$, we get a $8 \times 8$ $\mathbf{k}\cdot\mathbf{p}$ Hamiltonian as follows:

$$\mathbf{H_{k\cdot p}} = \begin{bmatrix} E_1 & \{ik_y\} & \{is_y\}+\{is_z\} & \{is_y\}+\{is_z\} & \{ik_x\} & \{ik_x\} & \{ik_x\} & \{is_y\}+\{is_z\} \\ & E_2 & \{ik_x\} & \{ik_x\} & \{is_y\}+\{is_z\} & \{is_y\}+\{is_z\} & \{is_y\}+\{is_z\} & \{ik_x\} \\ & & E_3 & \{is_x\} & \{E_z\}+\{ik_y\} & \{E_z\}+\{ik_y\} & \{E_z\}+\{ik_y\} & \{is_x\} \\ & & & E_4 & \{E_z\}+\{ik_y\} & \{E_z\}+\{ik_y\} & \{E_z\}+\{ik_y\} & \{is_x\} \\ & & & & E_5 & \{E_z\}+\{is_x\} & \{E_z\}+\{is_x\} & \{E_z\}+\{ik_y\} \\ & & & & & E_6 & \{is_x\} & \{E_z\}+\{ik_y\} \\ & & & & & & E_7 & \{E_z\}+\{ik_y\} \\ & & & & & & & E_8 \end{bmatrix}. \tag{A8}$$

Here we use $E_1 \ldots E_8$ to stand for the eigenvalue of Bloch states $\psi_1 \ldots \psi_8$ obtained by diagonalizing the Γ point Hamiltonian $H_0$. As we can see, there is a coefficient which is independent of perturbation strength before each element ($\{ik_{x,y}\}$, $\{is_{x,y,z}\}$, $\{iE_z\}$). It is worth noting that we can divide the set of Bloch states $\psi_1 \ldots \psi_8$ into weakly interacting subsets A (set of Bloch states $\psi_4$ and $\psi_5$) and B (set of Bloch states $\psi_1 \ldots \psi_3$ and $\psi_6 \ldots \psi_8$), such that we are interested in the subsets A whose Bloch states are near the Fermi level. In order to obtain the simplified Hamiltonian in the subset A, we can utilize the Löwdin transformation [30]. The fundamental concept of the Löwdin transformation is to transform the original Hamiltonian $H$ into a new Hamiltonian $\tilde{H}$, where the coupling matrix elements ($\langle\psi_m|\tilde{H}|\psi_l\rangle$) of the transformed Hamiltonian matrix $\tilde{H}$ are sufficiently small. Here, $|\psi_m\rangle(|\psi_l\rangle)$ represents Bloch state in the A(B) subset. By using Löwdin partitioning, we finally obtain the effective Hamiltonian in the basis $\psi_4$ and $\psi_5$ shown in Eq. (1).


[1] A. H. Castro Neto, F. Guinea, N. M. R. Peres, K. S. Novoselov, and A. K. Geim, Rev. Mod. Phys. **81**, 109 (2009).
[2] D. Akinwande, N. Petrone, and J. Hone, Nat. Commun. **5**, 5678 (2014).
[3] L. Li, Y. Yu, G. J. Ye, Q. Ge, X. Ou, H. Wu, D. Feng, X. H. Chen, and Y. Zhang, Nat. Nanotechnol. **9**, 372 (2014).
[4] R. A. Doganov, E. C. O'Farrell, S. P. Koenig, Y. Yeo, A. Ziletti, A. Carvalho, D. K. Campbell, D. F. Coker, K. Watanabe, T. Taniguchi *et al.*, Nat. Commun. **6**, 6647 (2015).
[5] D. A. Bandurin, A. V. Tyurnina, G. L. Yu, A. Mishchenko, V. Zolyomi, S. V. Morozov, R. K. Kumar, R. V. Gorbachev, Z. R. Kudrynskyi, S. Pezzini *et al.*, Nat. Nanotechnol. **12**, 223 (2017).
[6] K. F. Mak, C. Lee, J. Hone, J. Shan, and T. F. Heinz, Phys. Rev. Lett. **105**, 136805 (2010).
[7] D. Xiao, G.-B. Liu, W. Feng, X. Xu, and W. Yao, Phys. Rev. Lett. **108**, 196802 (2012).
[8] H. Ochoa and R. Roldán, Phys. Rev. B **87**, 245421 (2013).
[9] F. M. Kin, K. He, J. Shan, and F. H. Tony, Nat. Nanotechnol. **7**, 494 (2012).
[10] K. Taguchi, B. T. Zhou, Y. Kawaguchi, Y. Tanaka, and K. T. Law, Phys. Rev. B **98**, 035435 (2018).
[11] X. F. Qian, J. W. Liu, L. Fu, and J. Li, Science **346**, 1344 (2014).
[12] A. Lau, R. Ray, D. Varjas, and A. R. Akhmerov, Phys. Rev. Mater. **3**, 054206 (2019).
[13] J. H. Garcia, M. Vila, C.-H. Hsu, X. Waintal, V. M. Pereira, and S. Roche, Phys. Rev. Lett. **125**, 256603 (2020).
[14] M. Hu, G. Ma, C. Y. Wan, and J. Liu, Phys. Rev. B **104**, 035156 (2021).
[15] G. Kresse and J. Hafner, Phys. Rev. B **49**, 14251 (1994).
[16] G. Kresse and J. Furthmüller, Phys. Rev. B **54**, 11169 (1996).
[17] P. Hohenberg and W. Kohn, Phys. Rev. **136**, B864 (1964).
[18] W. Kohn and L. J. Sham, Phys. Rev. **140**, A1133 (1965).
[19] J. P. Perdew, K. Burke, and M. Ernzerhof, Phys. Rev. Lett. **77**, 3865 (1996).
[20] P. E. Blöchl, Phys. Rev. B **50**, 17953 (1994).
[21] G. L. Bir and G. E. Pikus, in *Symmetry and Strain-Induced Effects in Semiconductors* (Wiley, New York, 1974).
[22] R. Winkler, in *Spin-Orbit Coupling Effects in Two-Dimensional Electron and Hole Systems* (Springer, Berlin, 2003).
[23] J. C. Slater and G. F. Koster, Phys. Rev. **94**, 1498 (1954).
[24] V. M. Edelstein, Solid State Commun. **73**, 233 (1990).
[25] A. Dyrdał, J. Barnaś, and V. K. Dugaev, Phys. Rev. B **89**, 075422 (2014).
[26] A. Dyrdał and J. Barnaś, Phys. Rev. B **92**, 165404 (2015).
[27] M. Zhou, D. Zhang, S. Yu, Z. Huang, Y. Chen, W. Yang, and K. Chang, Phys. Rev. B **99**, 155402 (2019).
[28] C. H. Li, O. M. J. van't Erve, J. T. Robinson, Y. Liu, L. Li, and B. T. Jonker, Nat. Nanotechnol. **9**, 218 (2014).
[29] Supriyo Datta, in *Electronic Transport in Mesoscopic Systems* (Cambridge University Press, London, 1995).
[30] P.-O. Löwdin, J. Chem. Phys. **19**, 1396 (1951).